Selective Mercury Adsorption and Enrichment Enabled by Phenylic Carboxyl Functionalized Poly(pyrrole methane)s Chelating Polymers

Zhenyu Wang [a], Yunpeng Liu [a], Wenlong Zhang [a, c], Yubing Wang [a], Hao Xu [a], Liu Yang [a], Jiangtao Feng [a,e*], Bo Hou [b*], Mingtao Li [d], Wei Yan [a]

[a] Department of Environmental Engineering, Xi'an Key Laboratory of Solid Waste Recycling and Resource Recovery, School of Energy and Power Engineering, Xi'an Jiaotong University, Xi'an, 710049, China.

[b] School of Physics and Astronomy, Cardiff University, The Parade, Cardiff, CF24 3AA, UK

[c] School of Eco-Environment, Hebei University, Baoding 071002, China (present address)

[d] International Research Center for Renewable Energy (IRCRE), State Key Laboratory of Multiphase Flow in Power Engineering (MFPE), Xi'an Jiaotong University, Xi'an, Shaanxi 710049, China

[e] Jiangsu Engineering Laboratory of New Materials for Sewage Treatment and Recycling, Soochow University, Suzhou, Jiangsu 215123, China

Abstract: Mercury decontamination from water requires highly effective and efficient methods for maintaining public health and environmental protection. Herein, based on the

*Corresponding authors:

Jiangtao Feng: fjtes@xjtu.edu.cn; Bo Hou: HouB6@cardiff.ac.uk

coordination theory between functional groups and metal ions, we proposed phenylic carboxyl group-based poly(pyrrole methane)s (PPDCBAs) as highly efficient mercury removal materials for environmental remediation applications. It was found that PPDCBAs can efficiently adsorb and remove mercury(II) from aqueous solutions by functionalizing the molecular structure with phenylic carboxyl groups. Among the as-prepared PPDCBAs, poly[pyrrole-2, 5-diyl (4-carboxybenzylidane)] (PPD4CBA) with the carboxyl group at the *para* position can not only adsorb mercury over 1400 $mg \cdot g^{-1}$ but also achieve a 92.5% mercury(II) uptake within 100 minutes by a very low dosage of 0.1 $g \cdot L^{-1}$. In addition, PPDCBAs exhibited excellent adsorption selectivity for mercury(II) compared with copper(II), cadmium(II), zinc(II) and lead(II). Furthermore, as determined by Fourier transform infrared (FT-IR) spectra, X-ray photoelectron spectroscopy (XPS) and the density functional theory (DFT) calculation, the mercury removal was found to be mainly dependent on the high density of chelating sites, the phenylic carboxyl moieties, which helped us to realize an ultra-trace amount mercury removal (from 10.8 $\mu g \cdot L^{-1}$ to 0.6-0.8 $\mu g \cdot L^{-1}$) for meeting drinking water standard requirements (1.0 $\mu g \cdot L^{-1}$).

Keywords: poly(pyrrole methane)s, adsorption, mercury, carboxyl groups, density functional theory (DFT)

1. Introduction

Mercury(II) pollution, which can cause severe damage to the brain, kidneys and nervous system (Chen et al., 2021; Dai et al., 2019), has long been a threat to the ecosystem and further

public health by invading the human body through the food chain. Mercury is mainly generated from coal combustion, papermaking, oil refining and electroplating, metallurgy, and battery manufacturing (Dong et al., 2013; Velempini and Pillay, 2019; Wang et al., 2016) and exists in various chemical forms such as elemental mercury (Hg^0), inorganic mercury (Hg^{2+}) and methyl mercury (CH_3Hg^+) (Ballav et al., 2018; Holmes et al., 2009; Luo et al., 2015). In order to reduce the harm of mercury(II) to the environment and public health, the World Health Organization (WTO) sets the upper limit of mercury content in wastewater and drinking water as 5 $\mu g \cdot L^{-1}$ and 1 $\mu g \cdot L^{-1}$, respectively (Alguacil and López, 2020; Yan et al., 2021). In addition, according to the Minamata Convention in 2017, monitoring and controlling mercury pollution is imminent (Fu, Y. et al., 2019; Worthington et al., 2017). So it is imperative to develop effective technologies to remove the existing mercury pollution from water until the emissions can be significantly reduced.

Many technologies have been developed for mercury(II) removal from aqueous media, such as chemical precipitation (Brown; et al., 1979; Skyllberg and Drott, 2010), coagulation (Bachand et al., 2019; Henneberry et al., 2011), ion exchange (Alguacil and Escudero, 2020; Anirudhan et al., 2008), membrane separation (Chakrabarty et al., 2010; Mungray and Murthy, 2012) and adsorption (Ahmad et al., 2020; Nasimi et al., 2020). In comparison with other methods, adsorption is highly efficient, cost-effective, and environmentally friendly (Ballav et al., 2018). Various adsorbent materials, such as mesoporous silica (Fu, Y. et al., 2019; Gupta et al., 2019), chitosan (Ge and Du, 2020), cellulose (Bisla et al., 2020; Kenawy et al., 2018), carbon materials (Caicedo Salcedo et al., 2021), etc., have been applied to adsorb and remove

58 mercury(II) from wastewater. However, such prevalent adsorbents generally have low
59 adsorption capacity, poor selectivity and weak affinity for mercury(II). For example, the
60 specific surface area of activated carbon made from Mango seeds is 2-33 $m^2 \cdot g^{-1}$, and the
61 adsorption capacity of mercury(II) is only 56.1-85.6 $mg \cdot g^{-1}$ (Caicedo Salcedo et al., 2021). A
62 chemically guanyl-modified cellulose material has very poor adsorption selectivity for
63 mercury(II) (only 48 $mg \cdot g^{-1}$) (Kenawy et al., 2018). Therefore, the development of novel high-
64 efficiency adsorbents will be an important task.

65 Previous literature has shown that the introduction of suitable functional groups can
66 effectively improve the performance of adsorbents (Aguila et al., 2017; Duan et al., 2018; Fu,
67 L. et al., 2019; Li et al., 2019; Li et al., 2014; Zhao et al., 2019). The specific functional groups
68 can not only increase the uptake capacity but also improve the selectivity due to the different
69 affinity between functional groups and heavy metal ions. The sulfhydryl group (-SH) is highly
70 efficient as an adsorption site for mercury, which has been widely reported (Ballav et al., 2018;
71 Leus et al., 2017; Zhang et al., 2012; Zhao et al., 2019). However, the sulfhydryl group is less
72 stable, prone to be oxidized and forming disulfide bonds at higher pH conditions (Choi et al.,
73 2020; Monahan et al., 1995). The carboxylate group ($-COO^-$) is more stable, and can generally
74 coordinate with metal ions in three ways (Lawrance, 2013): only one oxygen is complexed
75 with one metal, each oxygen is combined with one metal separately, or two oxygen are
76 coordinated with one metal to form a more stable chelate. Therefore, we expect to obtain a
77 novel adsorbent that is easily regulated by carboxyl groups to remove mercury(II) from water
78 efficiently.

Conductive polymers, including polyaniline (PANI) (Lyu et al., 2019), polythiophene (PTh) (Chen et al., 2019) and polypyrrole (PPy) (Xu et al., 2019), have been used as a new type of adsorbent for efficient removal of heavy metal ions from water because of their good doping/dedoping performance and electrostatic interaction with heavy metal ions (Ji et al., 2021). Poly (pyrrole methane)s, a derivative of polypyrrole, is synthesized via the electrophilic substitution of α-H of pyrrole by protonated aldehydes under acid catalysis, which offers a feasible strategy to create a variety of active sites with good uptake capacities just by adding different aldehydes with functional groups. Furthermore, because of three different substitution sites on the benzene ring, poly(pyrrole methane)s synthesized from aromatic aldehyde can form three steric hindrance structures, which may affect the capture of mercury. Therefore, poly(pyrrole methane)s functionalized with phenylic carboxyl groups at different substitution sites could have distinct mercury capturing abilities. Systematic studies will be needed to determine the efficiency among these promising mercury(II) adsorbents.

In this study, poly[pyrrole-2, 5-diyl(benzylidane)] (PPDBA), poly[pyrrole-2, 5-diyl(2-carboxybenzylidane)] (PPD2CBA), poly[pyrrole-2, 5-diyl(3-carboxybenzylidane)] (PPD3CBA) and poly[pyrrole-2, 5-diyl(4-carboxybenzylidane)] (PPD4CBA) were designed and synthesized by one-step chemical polymerization. The as-prepared poly(pyrrole methane)s with carboxyl group in different substitution sites of benzene ring feature the highly accessible mercury(II) binding sites thereby affording strong adsorption selectivity for mercury(II) in the presence of other cations and the efficient mercury(II) capture capacity. The effects of typical anions and cations (e.g., Ca^{2+}, Na^{+}, K^{+}, Mg^{2+}, Cl^{-}, SO_4^{2-}, CO_3^{2-}, NO_3^{-}) on the Hg(II) removal

were also evaluated. Moreover, its practical application value is evaluated in real water matrices. Additionally, the mechanisms for Hg(II) removal are elucidated by the characterization (such as FT-IR, XPS) and density functional theory (DFT) calculations. This work reveals an effective strategy to tune the adsorption performance of poly(pyrrole methane)s as a potential efficient adsorbent for mercury removal.

2. Materials and Methods

2.1. Materials

Pyrrole (98%), benzaldehyde, 2-carboxybenzaldehyde, 3-carboxybenzaldehyde, 4-carboxybenzaldehyde, hydrochloric acid (HCl), sodium hydroxide (NaOH), nitric acid (HNO_3), N,N-Dimethylformamide (DMF), $Hg(NO_3)_2{\cdot}H_2O$, $Cd(NO_3)_2{\cdot}H_2O$, $Cu(NO_3)_2{\cdot}H_2O$, $Zn(NO_3)_2{\cdot}H_2O$, $Pb(NO_3)_2{\cdot}H_2O$, KNO_3, $Ca(NO_3)_2$, $Mg(NO_3)_2$, NaCl, Na_2SO_4 were purchased from Sinopharm Chemical Reagent Co., Ltd. All reagents were of analytical grade and used without further purification unless otherwise noted. And the deionized water used in this work was produced by EPED-40TF Superpure Water System (EPED, Nanjing, China).

2.2. Preparation of Poly(pyrrole methane)s.

The poly(pyrrole methane)s were synthesized by one-step chemical polymerization. First, 0.02 mol of benzaldehyde was dissolved in 100 mL DMF and poured into a 500 mL three-necked flask. After adding 28.6 mL of hydrochloric acid, 100 mL of DMF containing 0.02 mol of pyrrole was slowly added to the above solution, stirring at 350 rpm. Afterwards, the mixture liquid was kept stirring at 60°C for 6 hours, and then the solution was stirred at room

120 temperature for another 18 hours. Next, the mixture was poured into 800 mL of deionized water
121 with magnetic stirring for 10 minutes to precipitate the product, and then allowed to stand for
122 2 hours. The solid was filtered and washed with deionized water until the filtrate was neutral.
123 The solid obtained was dried at 60°C for 12 h, then ground into powder and sieved with a 100
124 mesh sieve, which is named "PPDBA". The above benzaldehyde was replaced by 2-
125 carboxybenzaldehyde, 3-carboxybenzaldehyde and 4-carboxybenzaldehyde to obtain
126 PPD2CBA, PPD3CBA and PPD4CBAa, respectively.

127 ***2.3. Characterizations***

128 Fourier transform infrared (FT-IR) spectra were scanned in the region of 500-4000 cm^{-1} using
129 KBr pellets on a Bruker TENSOR 37 FT-IR spectrophotometer. The pH values of the solution
130 were detected by a pH meter (FE28-Standard, Mettler Toledo). The morphology was examined
131 by scanning electron microscope (SEM, Zeiss Gemini SEM 500). The X-ray photoelectron
132 spectroscopy (XPS) spectra were performed on Kratos Axis Ultra DLD with an Al
133 monochromatic X-ray source (1486.71 eV), and all the binding energies (BEs) were revised
134 according to the C 1s hydrocarbon peak at 284.8 eV. The ^{1}H NMR spectra (Bruker III HD 400
135 M) were used to confirm the chemical structures of the as-prepared samples. The Barrett-
136 Emmett-Teller specific surface area (S_{BET}), total pore volume (V), and average pore radius (R)
137 were performed by a physical adsorption device (SSA-4200, Beijing Builder Co. Ltd, China).
138 Zeta potentials were determined on a Malvern Zetasizer Nano ZS90 at the pH value range of
139 2-12.

2.4. Batch Adsorption Studies

All solutions containing cations are prepared from corresponding nitrates in the adsorption experiments, and the solutions containing anions are corresponding sodium. The simulated solution used in the experiments was prepared by diluting the 5 mmol·L^{-1} $Hg(NO_3)_2$ stock solution with deionized water, and the initial pH value was adjusted by 0.1 mol·L^{-1} NaOH or HNO_3 solution. The 50 mL centrifuge tubes containing 2 mg adsorbent and 20 mL of 0.5 mmol·L^{-1} heavy metal ion solution were ultrasonically treated for 2 minutes to achieve uniform dispersion of the adsorbent in the liquid, and then transferred in a constant temperature shaker to adsorb at 220 rpm for 24 hours at 298 K. After the adsorption reaction, the solution filtered by a 0.45 μm-filter was analyzed by the inductively coupled plasma optical emission spectrometer (ICP-OES, ICPE-9000, Japan) to determine the concentration of heavy metal ions. The adsorption efficiency (η) and equilibrium adsorption capacity (Q_e) were calculated from the Eq. (1) and (2).(Liu et al., 2019)

$$\eta = \frac{C_0 - C_e}{C_0} \times 100\% \quad (1)$$

$$Q_e = \left(\frac{C_0 - C_e}{m} \right) V \quad (2)$$

where C_0 and C_e (mg·L^{-1}) are the initial and equilibrium concentrations of heavy metal ions in solution, respectively, m (g) is the adsorbent mass, and V (L) is the volume of solution.

For the kinetics study, 40 mg PPDCBAs were added to 10 mL of deionized water and the mixture was treated with ultrasound for 2 minutes, then poured into the 400 mL of 0.5 mmol·L^{-1} Hg(II) solution at pH 5-6. The reaction system was stirred with magnetic stirring at a speed

158 of 220 rpm and kept at 298 K with an oil bath. At time zero and preselected time intervals (0-
159 420 min), 2 mL samples were taken out and filtered quickly with polyethersulfone membrane
160 for Hg(II) concentration analysis.

161 To investigate the pH effect on Hg(II) removal by the as-prepared samples, the solution's
162 initial pH values were adjusted from 2 to 6 with 0.1 mol·L^{-1} HNO_3 or NaOH solution. Different
163 dosages are designed in the range of 0.05-1.0 g L^{-1} at an initial concentration of 100 mg·L^{-1}
164 (pH = 5.5, T = 25 °C) to study the effect of adsorbent dosage. In addition, adsorption isotherm
165 studies were carried out by changing the initial concentration of Hg(II) from 0.05 to 1 mmol·L^{-}
166 ^{1} at four different temperatures (288 K, 298 K, 308 K, 318 K).

167 The effect of background ions (Na^{+}, Ca^{2+}, Mg^{2+}, K^{+}, SO_4^{2-}, Cl^{-}) was investigated in a binary
168 adsorption mode, and the concentration of background ions was 10 mmol·L^{-1}. Furthermore, in
169 order to study the selective adsorption performance of the adsorbent, mixed solutions were
170 explored. The competitive heavy metal ions included Pb(II), Cd(II), Cu(II) and Zn(II), with the
171 same concentration of 0.5 mmol·L^{-1} of Hg(II).

172 In addition, batch adsorption-desorption experiments were carried out to investigate the
173 regeneration and reusability of PPDCBAs. Typically, 15 mg of PPDCBAs was mixed into 150
174 mL of Hg(II) solution (0.5 mmol·L^{-1}, pH=5.5). Then the desorption and regeneration of
175 exhausted PPDCBAs were accomplished with a 150 mL solution containing 0.1 mol·L^{-1} HCl
176 and 1 wt% thiourea and vibrating for 3 h at 298 K (Duan et al., 2018; Fu et al., 2022). Then,
177 the adsorbent was filtered and washed with deionized water until the filtrate was neutral for the
178 next adsorption-desorption cycle.

2.5. Density functional theory calculation details

The density functional theory (DFT) calculation was employed for further confirmation of the adsorption mechanism. The simulation was carried out by the Gaussian 09W software package using the B3LYP-D3 function, where D3 denotes the third-generation dispersion correction by Grimme. The solvation effect (H_2O) was evaluated with solvation model based on density (SMD) (Marenich et al., 2009). For structural optimization and frequency calculation, the 6-31+G(d) basis set was applied for the description of C, H, N, and O atoms, whereas the LANL2DZ basis set was used for Hg (Fu, T. et al., 2019). And static calculation was conducted using LANL2DZ basis set for Hg and 6-311++G(d, p) basis set for other atoms (Fu, T. et al., 2019; Zhao et al., 2019).

The adsorption energy (ΔE_{ad}) was calculated to evaluate the affinity between adsorbent materials and heavy metals by Eq. (3) (Oyetade et al., 2017).

$$\Delta E_{ad} = E_{complex} - (E_{metal} + E_{material}) \quad (3)$$

where $E_{complex}$, E_{metal} and $E_{material}$ are the energy ($kJ \cdot mol^{-1}$) of the metal ion-adsorbent complex, metal ion and adsorbent material, respectively.

3. Results and Discussion

3.1. Characterization of the poly(pyrrole methane)s

Fig. 1 exhibits the FT-IR spectra of the four poly(pyrrole methane)s. The peaks at around 3435 cm^{-1} are the N–H stretch of the pyrrole ring (Ji et al., 2021; Liu et al., 2019), the weak peaks at about 3100-3000 and 3000-2900 cm^{-1} are related to the C–H stretch of a benzene ring

198 and backbone (Liu et al., 2019), respectively. The C=C stretching of the benzene ring in
199 PPDBA, PPD2CBA, PPD3CBA and PPD4CBA appear at 1593, 1633, 1604 and 1608 cm^{-1},
200 respectively. The peaks at 1565 and 1407 cm^{-1} in PPDBA, 1576 and 1393 cm^{-1} in PPD2CBA,
201 1558 and 1387 cm^{-1} in PPD3CBA, 1540 and 1389 cm^{-1} in PPD4CBA are consistent with C=C
202 stretching and C–N stretching of the pyrrole ring, respectively (Anirudhan et al., 2008; Xu et
203 al., 2019). Compared with the PPDBA, the new adsorption bands at 3266, 1755 and 1287 cm^{-1}
204 in PPD2CBA, 3238, 1698 and 1266 cm^{-1} in PPD3CBA, 3258, 1699 and 1269 cm^{-1} in
205 PPD4CBA are attributed to –OH stretching, C=O stretching and C–O stretching of the carboxyl
206 group on the benzene ring, respectively (Ballav et al., 2018; Saleh, 2015; Xu et al., 2019).
207 However, it should be noted that the absorption peaks of –OH and C=O on the carboxyl group
208 of PPD2CBA are quite different from those on the other two samples, which is mainly caused
209 by the number of carboxyl groups. Since PPD3CBA and PPD4CBA contain more carboxyl
210 groups, hydrogen bonds are easily formed between the carboxyl groups, which will extend the
211 stretching peak of –OH to about 2500 cm^{-1}, and shift the stretching of C=O from 1755 to 1700
212 cm^{-1} (Bakker et al., 2003; I.D.Reva and S.G.Stepanian, 1995; Toru Yahagi et al., 2001). The
213 results of FT-IR indicated that the four poly(pyrrole methane)s were successfully synthesized
214 in this work.

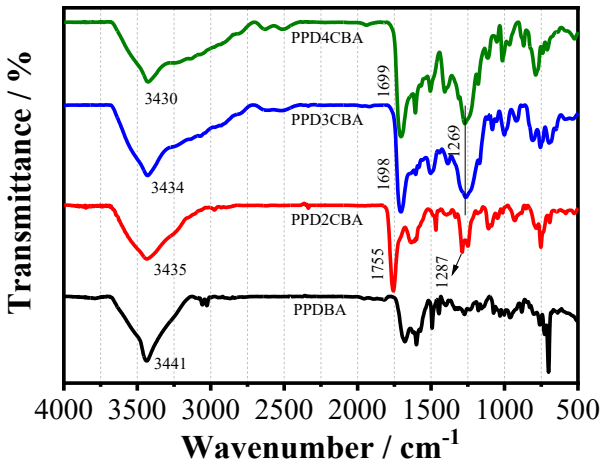

215

216 **Fig. 1.** FT-IR spectra of as-prepared PPDCBAs derivatives.

217 Fig. S1 shows the ^{1}H NMR spectra of the samples. PPDBA: ^{1}H NMR (500 MHz, DMSO-d_6,

218 δ): 10.87-10.12 (broad, 1H, NH), 7.84-6.59 (m, 7H, Pyr-H and Ar-H), 5.34 (s, 1H, $(Pyr)_2$-CH-

219 Ar). PPD2CBA: ^{1}H NMR (500 MHz, DMSO-d_6, δ): 12.38 (s, 1H, COOH), 11.25-10.87 (broad,

220 1H, NH), 7.93-6.62 (m, 6H, Pyr-H and Ar-H), 5.56 (s, 1H, $(Pyr)_2$-CH-Ar). PPD3CBA: ^{1}H NMR

221 (500 MHz, DMSO-d_6, δ): 12.95 (s, 1H, COOH), 10.86-10.12 (broad, 1H, NH), 8.45-6.89 (m,

222 6H, Pyr-H and Ar-H), 5.38 (s, 1H, $(Pyr)_2$-CH-Ar). PPD4CBA: ^{1}H NMR (500 MHz, DMSO-d_6,

223 δ): 12.94 (s, 1H, COOH),10.89-10.25 (broad, 1H, NH), 8.40-6.89 (m, 6H, Pyr-H and Ar-H),

224 5.38 (s, 1H, $(Pyr)_2$-CH-Ar) (Li et al., 2015). It is noted that the chemical shift of ^{1}H on the

225 carboxyl group in PPD2CBA is lower than that in PPD3CBA and PPD4CBA, which is because

226 more carboxyl groups in PPD3CBA and PPD4CBA strengthened the hydrogen bonds between

227 the sample molecules and reduced the shielding effect of active hydrogen, increasing the

228 chemical shift.

229 As depicted in Fig. S2, exposure of PPDCBAs to water at different pH (pH = 2-6) for 2 days

230 caused no obvious changes in molecular structure, which indicated that PPDCBAs had

231 excellent stability under the current pH range. In addition, TG curves showed that poly(pyrrole
232 methane)s still had good thermal stability when the temperature reached 200 °C (Fig. S3).
233 The elemental analysis result show that PPD4CBA and PPD3CBA have higher oxygen
234 content (Table 1), which means that they may contain more carboxyl groups, which is
235 consistent with the results of FT-IR and NMR. The oxygen in PPDBA may come from the
236 adsorbed water. The difference in oxygen content may be due to the influence of the spatial
237 position of carboxyl and aldehyde groups on the electrophilic substitution reaction in the
238 polymerization process.
239 **Table 1.** Content of C, N, H and O elements in the four prepared adsorbents

	Adsorbents	C%	N%	H%	O%
Test Value	PPDBA	81.25	8.47	5.20	1.9
	PPD2CBA	70.53	6.97	4.10	13.6
	PPD3CBA	67.18	6.43	4.42	18.4
	PPD4CBA	66.47	6.58	4.46	18.9
Theoretical Value	PPDBA	85.16	9.03	5.81	---
	PPDCBAs	72.36	7.04	4.52	16.08

240 The morphologies of the poly(pyrrole methane)s are characterized by SEM. As shown in Fig.
241 S4, all of them show irregular, short rod-shaped or spherical skeletons like aggregate. Pore
242 structure and specific surface area of the as-prepared poly(pyrrole methane) are shown in Table
243 S1 and Fig. S5. Obviously, PPD4CBA has a larger specific surface area (S_{BET}, 106.92 $m^2 \cdot g^{-1}$)
244 and pore volume (V, 0.76 $cm^3 \cdot g^{-1}$) than the other three samples.

3.2. Investigation of adsorption properties

3.2.1. Effect of initial pH

The impact of the initial pH of the solution on the adsorption is shown in Fig. 2a. The result indicates that the adsorption capacity of Hg(II) onto the poly(pyrrole methane)s is highly pH-dependent. The capture capacity increases with pH from 2 to 4 and reaches a plateau at pH from 4 to 7. Generally, for mercury ions, Hg^{2+} and $Hg(OH)^{+}$ are the dominant species in the solution at pH of 2-3 without Cl^{-} (Fig. 2b). Meanwhile, PPDCBAs are positively charged as their pH is below the pH_{zpc} (Fig. 2c). So, the low adsorption capacity for mercury at this pH may be attributed to electrostatic repulsion between positively charged mercury and adsorbent surface as well as the competition from H^{+} in the solution. With the increase of pH, mercury(II) is gradually converted to neutral $Hg(OH)_2(aq)$. The electrostatic repulsion with the adsorbent is negligible for the neutral $Hg(OH)_2(aq)$ is the dominant species at pH range 4-7.(Dong et al., 2013) Meanwhile, the complexation of $Hg(OH)_2(aq)$ with carboxylic groups in PPDCBAs is likely more favored because carboxylic groups became more deprotonated ($=COO^{-}$) at this pH range (Dong et al., 2013). Furthermore, $Hg(OH)_2$ has better mobility due to the smaller "effective molecular size" than Hg^{2+} and $Hg(OH)^{+}$ (Zhang et al., 2012).

3.2.2. Effect of dosage

The optimal adsorbent dosage is a critical parameter for the purification of wastewater by adsorption. Fig. 2d and Fig. S6 show the removal rate and adsorption capacity of Hg(II) with respect to the adsorbent dosage, respectively. The removal rate increases rapidly as a function

of dosages loading, which can be attributed to the increase of available adsorption sites. Eventually, the removal rate of mercury gradually reaches 100% for PPDCBAs. However, the removal rate of Hg(II) remains basically invariant for PPDBA as the dosage increases, owing to fewer adsorption sites of PPDBA. Furthermore, even at a low dosage (0.1 $g \cdot L^{-1}$), the removal rate of Hg(II) by PPD3CBA and PPD4CBA can still reach above 90%, and PPDCBAs maintain high adsorption capacity. Therefore, the dosage of 0.1 $g \cdot L^{-1}$ was chosen as a standard in the following experiments.

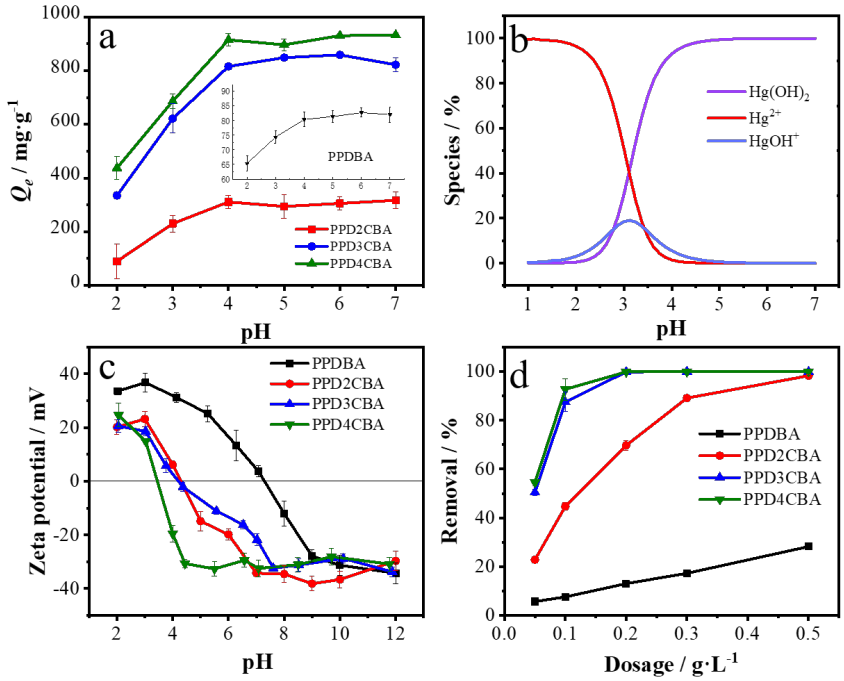

Fig. 2. Effect of initial solution pH on the Hg(II) adsorption (C_0 = 100 $mg \cdot L^{-1}$, dosage = 0.1·$g \cdot L^{-1}$, T = 298 K, pH = 2-7) (a), Morphological distribution of Hg(II) at different pH in the absence of chloride (b), Zeta potentials of the adsorbents (c), Effect of dosage on the removal of Hg(II) (C_0 = 100 $mg \cdot L^{-1}$, dosage = 0.05-0.5·$g \cdot L^{-1}$, T = 298 K, pH=5.5) (d).

277 *3.2.3. Adsorption kinetics*

278 The influence of the contact time on Hg(II) adsorption by PPDCBAs is shown in Fig. 3a.
279 Hg(II) adsorption onto PPDCBAs increased rapidly in the initial 30 min and reached a plateau
280 afterwards. And the initial adsorption rate of three PPDCBAs followed the order of PPD4CBA
281 > PPD3CBA > PPD2CBA. The adsorption equilibrium of the PPDCBAs reached within 100
282 min.

283 Pseudo-first-order (PFO) model and pseudo-second-order (PSO) model are always employed
284 to evaluate the kinetic data. The differential form of the PFO model and PSO model are
285 described in Eq. (4) and (5) (Wang and Guo, 2020), respectively.

$$\frac{dQ_t}{dt} = k_1(Q_e - Q_t) \tag{4}$$

$$\frac{dQ_t}{dt} = k_1(Q_e - Q_t)^2 \tag{5}$$

286 where Q_t (mg·g^{-1}) and Q_e (mg·g^{-1}) are the adsorption capacity at time t (min) and equilibrium
287 respectively, k_1 (min^{-1}) and k_2 (g·mg^{-1}·min^{-1}) are the rate constants for the pseudo-first-order and
288 pseudo-second-order, respectively.

289 Integrating Eq. (4) and (5) for the conditions of $Q_0 = 0$ yields Eq. (6) and (7), respectively.

$$Q_t = Q_e(1 - e^{-k_1 t}) \tag{6}$$

$$Q_t = \frac{k_2 Q_e^{\,2} t}{1 + k_2 Q_e t} \tag{7}$$

290 PFO and PSO models are applicable to three different hypotheses and conditions,
291 respectively. Firstly, the high C_0 value is applicable to the PFO model, while the low C_0 value
292 is applicable to PSO model; Secondly, PFO model can better describe the initial stage of the

adsorption process, while PSO model is more suitable for the adsorption process at the final stage; Finally, the adsorption materials with few adsorption sites can be better described by PFO model. Therefore, the adsorption is not only determined by the active sites, and in some cases, the PFO model can be dominated by external/internal diffusion. However, the adsorption materials with abundant active sites can be well modelled by the PSO model, which means the adsorption kinetics is dominated by the adsorption onto the active site (Wang and Guo, 2020).

In addition, the Elovich model has been extensively applied to chemisorption data, which was described by Eq. (8) (Elovich and Larinov, 1962; Tran et al., 2017).

$$\frac{dQ_t}{dt} = \alpha e^{-\beta Q_t} \tag{8}$$

where α (mg·g^{-1}·min^{-1}) reflects the initial adsorption rate because $dQ_t/dt \rightarrow \alpha$ when $Q_t \rightarrow 0$, and β (mg·g^{-1}) is the desorption constant during any one experiment.

By applying the boundary conditions of $Q_t = 0$ at $t = 0$, the integrated form of Eq. (8) will become Eq. (9)

$$Q_t = \frac{1}{\beta}\ln(1+\alpha\beta t) \tag{9}$$

Table S2 depicts the kinetic parameters for the three models. It can be observed that the PSO (R^2 = 0.9518-0.9703) could better describe the adsorption kinetics of PPDCBAs for Hg(II) compared with PFO (R^2 = 0.8920-0.9112), suggesting that the adsorption kinetics is dominated by the adsorption onto the active site. The Elovich model with the larger correlation coefficients (R^2 = 0.9829-0.9987) further indicated that the adsorption of Hg(II) onto PPDCBAs involved a chemical adsorption process. Moreover, the relatively bigger rate constant α indicated that PPD4CBA had a higher initial adsorption rate (Lin et al., 2018).

In addition, the diffusion mechanism was further evaluated by analyzing the role of intra-particle diffusion in the adsorption process. The linearized transformation of the intra-particle diffusion model is presented as Eq. (10) (Tran et al., 2017).

$$Q_t = k_i t^{\frac{1}{2}} + C_i \tag{10}$$

where k_i ($mg \cdot g^{-1} \cdot min^{-1/2}$) is the intra-particle diffusion rate constant and C_i ($mg \cdot g^{-1}$) is a constant associated with the thickness of the boundary layer, where a higher value of C_i corresponds to a greater effect on the limiting boundary layer.

Linear plots of the intra-particle diffusion model for all three adsorbents are depicted in Fig. 3b. It can be seen that the adsorption process can be divided into three linear regions with different slopes, which indicates that the adsorption process is affected by multiple diffusion steps. The initial sharp linear region could be attributed to the surface adsorption of Hg(II), which was controlled by boundary layer diffusion. In the second stage, the adsorption rate slowed down gradually, indicating that intra-particle diffusion was the rate-limiting mechanism during this stage. In the last stage, due to the decrease in the Hg(II) concentration in solution, the diffusion rate in the particles further slowed down, thus reaching the final equilibrium stage.

3.2.4. Adsorption isotherm

Adsorption isotherms play a vital role in evaluating the adsorption capacities of adsorbents and investigating chemical interactions between adsorbate and adsorbents. Langmuir and Freundlich isotherms are widely used to analyze the adsorption isotherm data, and their non-linear formulas are given by Eq. (11) and (12), respectively (Al-Ghouti and Da'ana, 2020;

Zhang, Y. et al., 2021). The basic assumptions of the Langmuir isotherm are: (1) monolayer adsorption; (2) the distribution of adsorption sites is homogeneous; (3) the adsorption energy is constant; and (4) the interaction between adsorbate molecules is negligible. And the Freundlich equation is one of the earliest empirical equations used to describe equilibrium data and adsorption characteristics for a heterogeneous surface (Freundlich, 1907). Unlike the Langmuir isotherm model, Freundlich model is not restricted to the monolayer formation in which its application to the multilayer adsorption is possible (Al-Ghouti and Da'ana, 2020).

$$Q_e = \frac{Q_{\max} K_L C_e}{1 + K_L C_e} \tag{11}$$

$$Q_e = K_F C_e^{1/n} \tag{12}$$

where C_e ($mg \cdot L^{-1}$) is the heavy metal ion concentration at adsorption equilibrium; Q_e ($mg \cdot g^{-1}$) and $Q_{\max}$ ($mg \cdot g^{-1}$) are the equilibrium adsorption capacity and the maximum monolayer adsorption capacity, respectively; K_L ($L \cdot mg^{-1}$) is the Langmuir constant which is related to the affinity of adsorbate and the binding sites; K_F ($(mg \cdot g^{-1})/(mg \cdot L^{-1})^{1/n}$) is the Freundlich constant indicating the relative adsorption capacity of the adsorbents. n is a dimensionless constant related to the intensity of adsorption.

In addition, the dimensionless separation factor R_L can estimate the favorability of the adsorption and is expressed by Eq. (13) (Al-Ghouti and Da'ana, 2020; Hall et al., 1966).

$$R_L = \frac{1}{1 + K_L C_0} \tag{13}$$

where C_0 ($mg \cdot L^{-1}$) is the initial concentration of adsorbate. The value of R_L indicates irreversible adsorption when $R_L = 0$, favorable adsorption when $0 < R_L < 1$, linear case when $R_L = 1$ or unfavorable adsorption when $R_L > 1$.

According to Fig. 3c-e and Table S3, Langmuir model fits better than the Freundlich model for all PPDCBAs, suggesting that the adsorption process is monolayer adsorption.(Xu et al., 2019) Meanwhile, according to the calculation based on experimental data, the values of R_L are in the range of 0 to 1, which indicates the adsorption process is favorable under operating conditions (Al-Ghouti and Da'ana, 2020). Moreover, as the temperature increases from 288 K to 328 K, the maximum adsorption capacity (Q_{max}) of Hg(II) onto PPD2CBA, PPD3CBA and PPD4CBA increased from 406.82 to 875.14 $mg \cdot g^{-1}$, from 862.62 to 1234.66 $mg \cdot g^{-1}$ and from 919.75 to 1427.18 $mg \cdot g^{-1}$, respectively. In conclusion, it is believed that Hg(II) adsorption is achieved by forming monolayers on the limited adsorption sites on the homogeneous surface (Xu et al., 2019). The comparisons of the adsorption performance of various adsorbents for Hg(II) are shown in Fig. S7 and Table S4. The PPDCBAs offer good adsorption properties for Hg(II) with a very low usage dose (0.1 $g \cdot L^{-1}$) at a wide pH range.

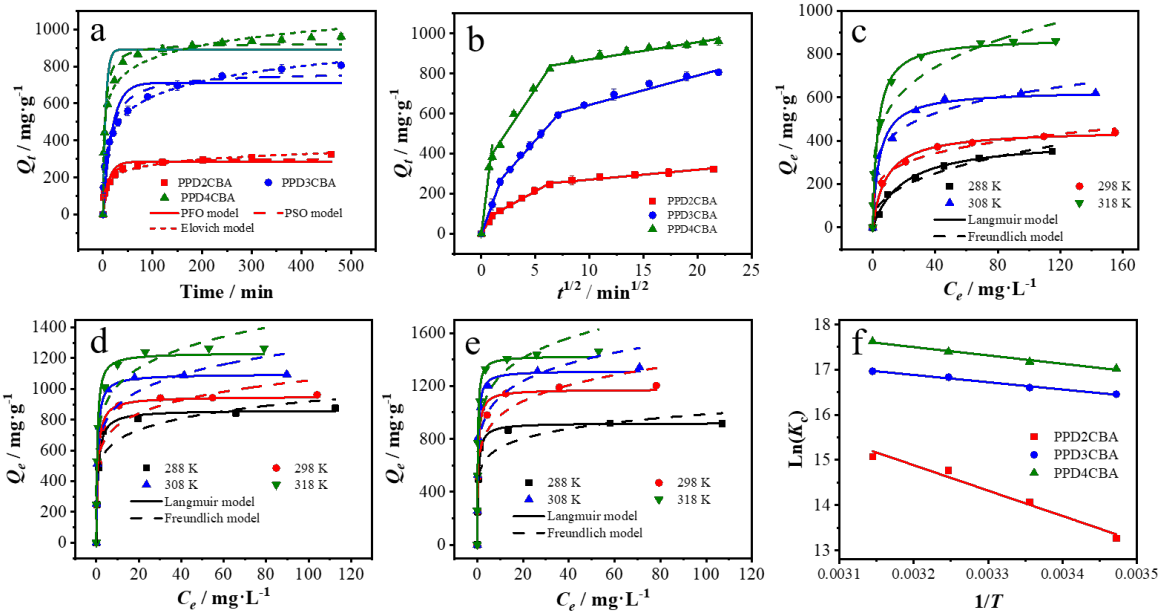

361

362 **Fig. 3.** Adsorption kinetics plots and fitting curves of Hg(II) onto PPDCBAs (a), intra-particle

363 diffusion model for adsorption of Hg(II) onto PPDCBAs (b)(C_0 = 100 mg·L^{-1}, Dosage =

364 0.1·g·L^{-1}, T = 298 K, pH=5.5), adsorption isotherms for the adsorption of Hg(II) onto

365 PPD2CBA, PPD3CBA and PPD4CBA (c-e) (C_0 = 100 mg·L^{-1}, dosage = 0.1·g·L^{-1}, T = 288-

366 318 K, pH = 5.5), the plots to determine the thermodynamic parameters of Hg(II) adsorption

367 onto PPDCBAs (f).

368 *3.2.5. Thermodynamic parameters*

369 According to Fig. 3c-e and Table S3, the maximum adsorption capacities increase with

370 increasing temperature. Thermodynamic parameters, such as entropy change (ΔS, kJ·mol^{-1}·K^{-1}), enthalpy change (ΔH, kJ·mol^{-1}) and the standard free energy change (ΔG, kJ·mol^{-1}) can be

372 derived based on Eq. (14-16) (Tran et al., 2017; Zhou and Zhou, 2014).

$$\ln K_C = \frac{-\Delta H}{RT} + \frac{\Delta S}{R} \tag{14}$$

$$K_C = \ln(M_W \times 55.5 \times 1000 \times K_L) \quad (15)$$

$$\Delta G = \Delta H - T\Delta S \quad (16)$$

where K_C is a dimensionless standard equilibrium constant. 55.5 is the mole concentration of water in $mol \cdot L^{-1}$, K_L is the Langmuir constant in $L \cdot g^{-1}$, and M_W ($g \cdot mol^{-1}$) is the molecular weight of the adsorbate. R (8.314 $J \cdot mol^{-1} \cdot K^{-1}$) is the universal gas constant, and T is the temperature in K.

ΔS and ΔH are calculated from the intercept and slope of the plot of ln K_d versus $1/T$ (Fig. 3f). The obtained values of ΔG, ΔH and ΔS under different temperatures are listed in Table S5. The negative ΔG and positive ΔH indicate that the Hg(II) adsorption process is spontaneous and endothermic (Xu et al., 2019). And the positive values of ΔS indicate that the randomness at the solid-liquid interface increases in the adsorption process of Hg(II) (Liu et al., 2019). Moreover, the ΔG values decrease with increased temperature, suggesting increased spontaneity with temperature.

3.2.6. Effect of the co-existing ions on Hg(II) adsorption

In addition to heavy metals, other ions (e.g., Ca^{2+}, Na^{+}, K^{+}, Mg^{2+}, Cl^{-}, SO_4^{2-}, NO_3^{-}) widely exist in various water bodies, which may have a negative impact on the adsorption process. In view of this, the effect of selected ions (Na^{+}, K^{+}, Ca^{2+}, Mg^{2+}, Cl^{-}, SO_4^{2-}) on the removal of Hg(II) by PPDCBAs was studied. As shown in Fig. 4a, the co-existing ions such as Na^{+}, K^{+}, Ca^{2+}, Mg^{2+}, and SO_4^{2-} do not impact Hg(II) adsorption, which also indicates that NO_3^{-} has no effect on the adsorption of mercury because the cations are all from the corresponding nitrate. However, Cl^{-} has an apparent inhibitory effect, which is consistent with the literature reports

(Jainae et al., 2015; Zhu et al., 2017). This is because mercury species are complicated by the high chloride ion concentration (10 mmol·L^{-1} NaCl) (Fig. 4b) (Jainae et al., 2015; Lu et al., 2014; Zhu et al., 2017). According to the calculation, under the condition of pH = 5-6, Cl^- and Hg(II) will form multiple complexes, in which $HgCl_2$ is the dominant species, reaching nearly 90%, $HgCl_3^-$ accounts for nearly 10%, but $Hg(OH)_2$ and HgClOH are trace amounts. Then different concentrations of NaCl are added to further explore the effect of Cl^- on Hg(II) adsorption. Fig. 4c shows the adsorption capacity of PPD4CBA for Hg(II) and the morphological distribution of Hg at pH=5.5 at different Cl^- concentrations, respectively. As the concentration of Cl^- increases, the adsorption capacity has the same trend with $Hg(OH)_2$ content but the opposite trend with $HgCl_2$ content, indicating that $Hg(OH)_2$ is an important species to be adsorbed but $HgCl_2$ is hardly adsorbed. In addition, when the concentration of Cl^- is 1.0 mmol, the amount of $Hg(OH)_2$ only accounts for 2%, but PPD4CBA still has an adsorption capacity of more than 440 mg·g^{-1}, indicating that HgClOH may contribute a part of the adsorption capacity. And as shown in Fig. 4d, the adsorption capacity of PPD4CBA for Hg(II) has a good positive linear relationship with the percentage of $Hg(OH)_2$ plus HgClOH, which further indicates that $Hg(OH)_2$ and HgClOH are active species and have much stronger affinity with the adsorbent than $HgCl_2$. On the one hand, $Hg(OH)_2$ and HgClOH has a smaller "effective molecular size" and higher mobility than $HgCl_2$ (Afaneh et al., 2012; Nightingale, 1959). On the other hand, $Hg(OH)_2$ is more accessible to interact with the active adsorption sites due to the hydrogen bond between hydroxyl and carboxyl (Zhang et al., 2020).

Selectivity is an important parameter for adsorbents in practical applications since several co-existing heavy metal ions may also be present in Hg(II)-containing wastewater. Therefore, the possible interference of various co-existing ions (Cu(II), Cd(II), Pb(II), and Zn(II)) on Hg(II) adsorption was investigated. As noted in Fig. 4e, PPDCBAs exhibit high adsorption selectivity for Hg(II), and competition from co-existing ions rarely disturbs the adsorption of Hg(II). The results show that PPDCBAs have a much stronger affinity for Hg(II). In addition, distribution coefficients (K_d, $L \cdot g^{-1}$) and selectivity coefficient (α) calculations were calculated to investigate the affinity and selectivity degree of adsorbents. The large K_d values indicate that PPDCBAs can well remove the metal ions. K_d and α could be illustrated as Eq. (17, 18) (Lin et al., 2019; Wang et al., 2014).

$$K_d = \frac{Q_e}{C_e} \tag{17}$$

$$\alpha = \frac{K_d(Hg)}{K_d(M_i)} \tag{18}$$

where $K_d(Hg)$ and $K_d(M_i)$ represent the distribution coefficients of Hg(II) and co-existing ions, respectively.

As noted in Table 2, the K_d value of Hg(II) exceeds that of interfering ions, suggesting that PPDCBAs have an adsorption affinity for Hg(II) that surpasses interfering ions by a wide margin. In addition, the adsorption capacity of PPDCBAs for Cu(II) and Pb(II) is slightly higher than that of Cd(II) and Zn(II), which is related to the existence form of ions under experimental conditions. Cu(II) and Pb(II) form part of hydroxide, while Cd(II) and Zn(II) basically exist in the form of M^{2+} at pH = 5-6 (Fig. S8). This illustrates that PPDCBAs have a

stronger affinity for the complex of heavy metals and hydroxide than other M^{2+}, which further proves the effect of initial pH on mercury adsorption.

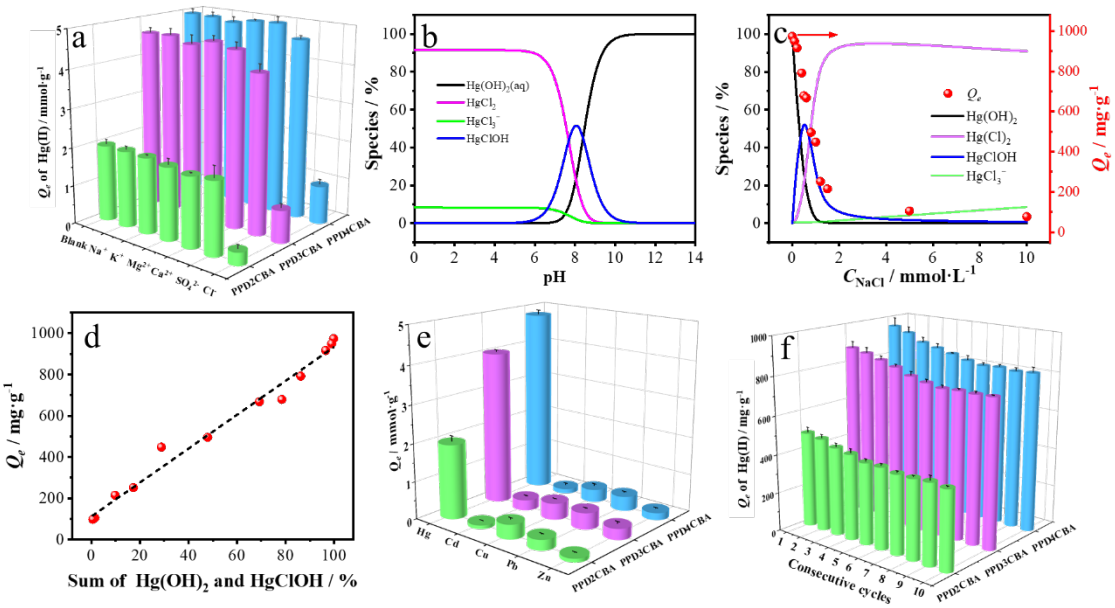

Fig. 4. Effect of background ions on the removal of Hg(II) by PPDCBAs (C_0 = 0.5 mmol·L^{-1}, dosage = 0.1·g·L^{-1}, T = 298 K, pH = 5.5, the concentration of background ions is 10 mmol·L^{-1}) (a), Morphological distribution of Hg(II) at different pH at NaCl concentration of 10 mmol·L^{-1} (b), Adsorption capacity of PPD4CBA for Hg(II) and the morphological distribution of Hg at pH=5.5 at different Cl^- concentrations (c), The linear relationship between the adsorption capacity of PPD4CBA and the ratio sum of $Hg(OH)_2$ and HgOHCl (d), Effect of co-existing heavy metal ions on the removal of Hg(II) by PPDCBAs (C_M = 0.5 mmol·L^{-1}, dosage = 0.1·g·L^{-1}, T = 298 K, pH = 5.5) (e), Adsorption-desorption cycles of Hg(II) onto PPDCBAs (f).

Table 2. The distribution coefficient and selectivity coefficient of heavy metal adsorbed by PPDCBAs

Metal ions	PPD2CBA	PPD3CBA	PPD4CBA

	K_d (L·g^{-1})	α	K_d (L·g^{-1})	α	K_d (L·g^{-1})	α
Hg	6.12	—	34.12	—	127.02	—
Pb	0.64	9.53	1.05	32.38	0.93	137.18
Cu	0.94	6.50	1.06	32.07	0.81	155.88
Zn	0.19	32.46	0.59	58.01	0.37	339.53
Cd	0.19	31.57	0.57	60.21	0.25	511.72

3.3. Evaluation of real application

Compared with other heavy metals, the emission limit of mercury in drinking water is more stringent. Less than 1 μg·L^{-1} is restricted by WHO. The adsorption method is commonly used in the advanced treatment of heavy metal wastewater, and the initial mercury content is usually very low (Fu et al., 2022; Richard and Biester, 2016). It is hoped that the adsorbent can remove the low mercury concentration below the emission limit. As shown in Table 3, the concentration of mercury in the solution can be reduced to less than 1 μg·L^{-1} after adsorption, which indicates that PPDCBAs can remove trace Hg(II) effectively, proving their potential value in practical applications.

To deeply determine the real application potential of PPDCBAs on Hg(II) removal, the performance of PPDCBAs was further investigated in tap water and Weihe River water matrices. The concentrations of typical anions (e.g., F^-, Cl^-, SO_4^{2-}, NO_3^-, etc.) and COD are shown in Table S6. As the typical Hg(II) concentrations in surface water/groundwater range from 0.001 to 0.87 mg·L^{-1}, therefore, the tap water and Weihe river water were spiked with 0.1 mg·L^{-1} and 0.3 mg·L^{-1} Hg(II), respectively. As displayed in Table 3, over 95% of Hg(II) was

successfully removed by PPDCBAs. Based on the above results, the applicability of PPDCBAs to remove Hg(II) in real water matrices is fully validated.

Table 3 Removal result of trace mercury in different types of water by PPDCBAs.

Water type	pH		The concentration of Hg(II)[a] / μg·L^{-1}		
			PPD2CBA	PPD3CBA	PPD4CBA
Deionized water	6.74	Before adsorption		10.8	
		After adsorption	0.739	0.827	0.623
		Removal rate / %	93.1	92.3	94.2
Tap water	7.88	Before adsorption		107	
		After adsorption	---	5.18	5.30
		Removal rate / %	---	95.2	95.0
Weihe River water	7.98	Before adsorption		313	
		After adsorption	---	11.4	12.0
		Removal rate / %	---	96.4	96.2

[a] The concentration of mercury was detected by inductively coupled plasma mass spectrometer.(ICP-MS, NexION 350D)

The regeneration performance of the adsorbent is of great significance in evaluating the practical application value. In many reports, mixed solutions of acid and thiourea have been used to achieve effective desorption of mercury (Duan et al., 2018; Fu et al., 2022). On the one hand, thiourea, as a small molecule substance rich in sulfur and nitrogen, has a very strong binding ability with mercury. On the other hand, desorption is a reverse process of adsorption, and conditions unfavorable to adsorption must be favorable conditions for desorption. In our study, lower pH and Cl^- effectively inhibit the adsorption of mercury, so batch regeneration studies were carried out using the mixed solution of 0.1 mol • L^{-1} HCl and 1.0 wt% thiourea as

471 the desorption agent. Adsorption-desorption experiments were performed for ten consecutive
472 cycles to evaluate the regeneration efficiency of PPDCBAs (Fig. 4f). After ten adsorption-
473 desorption cycles, the results show that PPDCBAs still maintain more than 85% of their
474 original adsorption capacity, confirming their adsorption stability.

475 ***3.4. Mechanism of the Hg(II) adsorbed onto PPDCBAs***

476 The experimental results show that PPDCBAs have a much higher adsorption capacity than
477 that of PPDBA, indicating that the introduction of the carboxyl group significantly improved
478 the performance of the adsorbent, which is in agreement with previous studies (Li et al., 2019;
479 Peng et al., 2018). Meanwhile, the extracted adsorption capacities of PPDCBAs are in the
480 following order: PPD4CBA > PPD3CBA > PPD2CBA, which agrees with the ranking of
481 oxygen content in the results of elemental analysis (please see Table 1). Clearly, in the
482 adsorption process, carboxyl groups play a critical role.

483 The PPDCBAs before and after adsorption were analyzed using FT-IR. As shown in Fig. 5,
484 the C=O stretching of PPD2CBA (1755 cm^{-1}) is significantly weakened, and the C=O
485 stretching of PPD3CBA (1698 cm^{-1}) and PPD4CBA (1699 cm^{-1}) are disappeared. At the same
486 time, the C−O stretching of the carboxyl group (1287 cm^{-1} for PPD2CBA, 1266 cm^{-1} for
487 PPD2CBA, 1269 cm^{-1} for PPD4CBA) almost disappear after Hg(II) adsorption. These changes
488 indicate that Hg(II) interacts with carboxyl groups on the surface of PPDCBAs.

489 The XPS spectra were also employed to explore the adsorption mechanism (Fig. 6). In the
490 full-scan spectrum (Fig. 6a-c), the new peaks (Hg 4f) are observed after absorption of Hg(II),
491 and as described in Fig. 6d-f, the binding energy of Hg 4f could be split into two different peaks

492 at 105.59-105.73 eV and 101.55-101.69 eV, which turns out that Hg(II) have been successfully
493 adsorbed by PPDCBAs (Duan et al., 2018; Lin et al., 2019). Fig. 6g shows the high resolution
494 of O 1s peak of PPD2CBA before and after Hg(II) adsorption. The binding energy of C=O
495 (533.60 eV) and C−O (532.36 eV) (Gao et al., 2019) are changed to 532.97 eV and 531.82 eV
496 after adsorbing mercury, respectively, indicating that the oxygen-containing functional groups
497 are complexed with Hg(II). Similar results appear in Fig. 6h and i, which represent the
498 adsorption of Hg(II) onto PPD3CBA and PPD4CBA, respectively. In Fig. 6j, the binding
499 energy of PPD2CBA at 400.84, 400.34 and 398.41 eV, assigning to $-N^{+}-$, −NH− and −N= (Liu
500 et al., 2019), are shifted to 400.63, 399.65 and 397.98 eV after adsorption, respectively. These
501 changes indicate that nitrogen atoms are also involved in Hg(II) adsorption onto PPD2CBA.
502 Similarly, Fig. 6k and Fig. 6l also share the same conclusion.
503 Moreover, the pH value of the solution after adsorption declined slightly when the initial pH
504 was 2-3. However, the pH value after adsorption increased when the initial pH was 4-7 (Table
505 4). Hence, we speculate that the mercury removal mechanism can be represented by the
506 following complexation between carboxyl groups and Hg(II), as shown in Fig. 7. First, when
507 the pH is low, the main species Hg^{2+} were captured by the carboxyl group (=COOH), and
508 hydrogen ions are released after complexation, which leads to a decrease in the pH of the
509 solution. Then as the pH increases, $Hg(OH)_2$ and $HgOH^{+}$, which gradually became the
510 dominant species, are trapped by the active site under hydrogen bonding and electrostatic
511 attraction, then Hg^{2+} is chelated with the carboxyl group, and OH^{-} is released at the same time,
512 resulting in an increase in the pH of the solution. Based on the discussion in Section 3.2.6,

HgClOH and $HgCl_2$ are the main active species when Cl^- is present, and the adsorption process is depicted in Fig. S10.

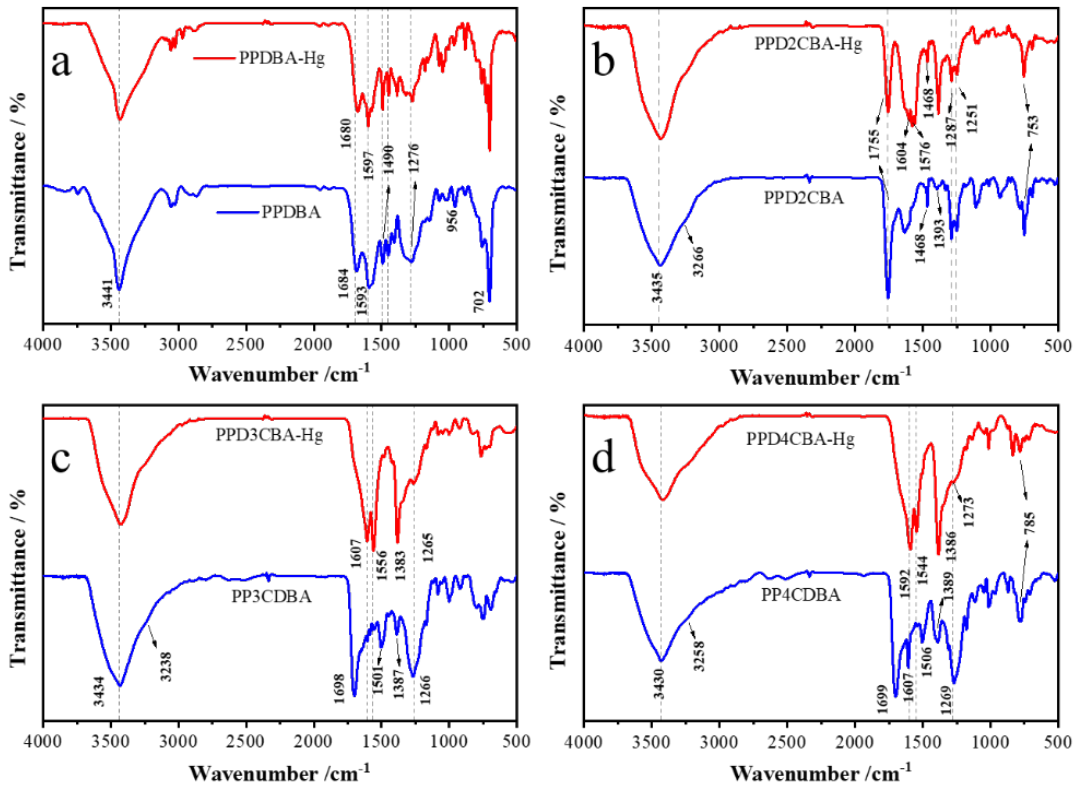

Fig. 5. FT-IR spectra of the samples before and after adsorption: PPDBA (a), PPD2C BA (b), PPD3CBA (c) and PPD4CBA (d).

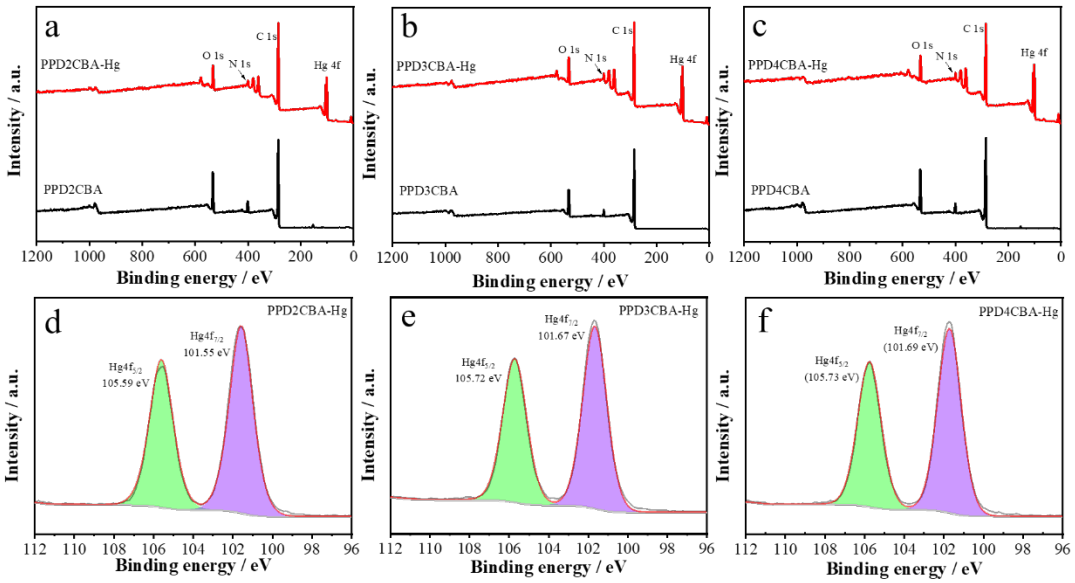

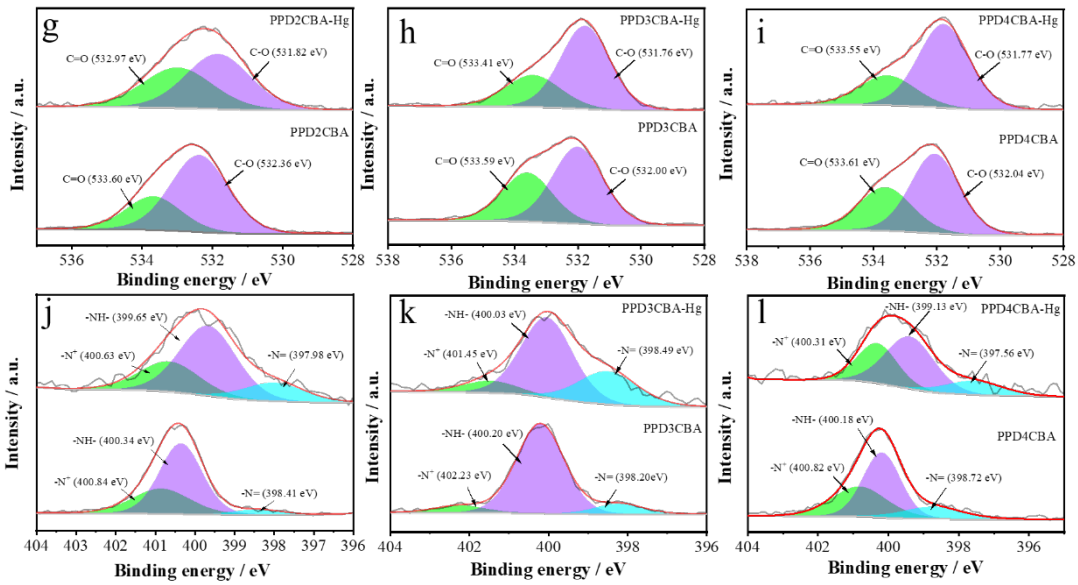

519

520 **Fig. 6.** Full scan survey XPS spectra: PPD2CBA (a), PPD3CBA (b) and PPD4CBA (c), High

521 resolution spectra of Hg 4f (d-f), O 1s (g-i) and N 1s (j-l) of PPD2CBA, PPD3CBA and

522 PPD4CBA before and after Hg(II) adsorption.

523 **Table 4.** Variation of solution pH before and after mercury adsorption

Adsorbents / Initial pH	PPDBA	PPD2CBA	PPD3CBA	PPD4CBA
2	2	2.01	2	2
3	3.02	2.98	2.89	2.88
4	4.28	4.28	4.32	4.19
5	7.38	6.21	6.45	6.09
6	8.15	7.09	6.51	6.30

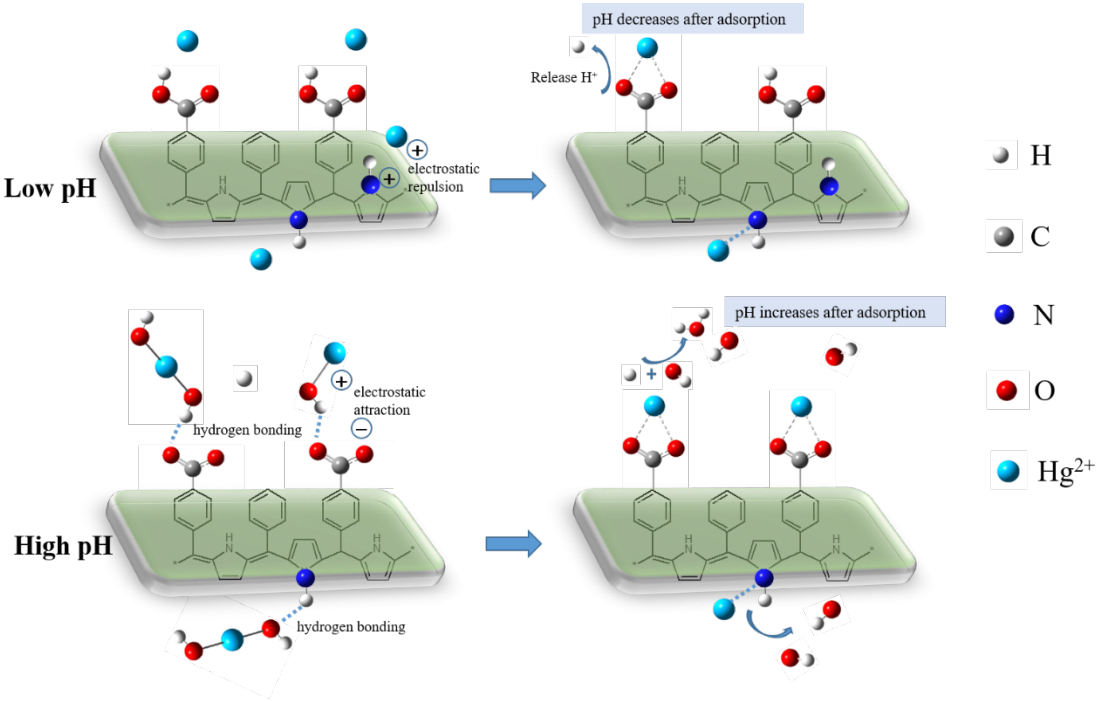

524

525 **Fig. 7.** Possible interactions between carboxyl groups and Hg(II).

526 DFT calculation was also employed to further confirm the adsorption mechanism. The
527 optimized geometries of the possible complexes formed by poly(pyrrole methane)s with Hg(II)
528 are presented in Fig. 8, and the calculation results are summarized in Table 5. It can be seen
529 that the adsorption energy between the Hg(II) and carboxyl group (from -79.66 to -83.83
530 kJ·mol^{-1}) is more negative compared with that of the imino group (from -57.29 to -68.54 kJ·mol^{-}
531 ^{1}), indicating that the carboxyl groups have a stronger affinity to mercury and play a major role
532 in the mercury capture process, which is consistent with the results of FT-IR analysis. In
533 addition, it can be concluded that the affinity between mercury and the carboxyl group in
534 PPDCBAs confirms the following order: PPD4CBA > PPD3CBA > PPD2CBA, which is
535 consistent with the experimental results of the adsorption capacity. In addition, we further
536 calculated to compare the Mulliken charge distribution of PPDCBAs before and after Hg(II)

adsorption (Takjoo et al., 2016; Tellez et al., 2016; Zhang, Z. et al., 2021). Based on the structure-optimized PPDCBAs, Hg^{2+} and complexes of PPDCBAs and Hg^{2+}, static calculations were carried out and obtained the Mulliken charges of mercury in the PPD2CBA-Hg(II), PPD3CBA-Hg(II) and PPD4CBA-Hg(II) to be +1.5254, +1.5149 and +1.5168 *e*, respectively. Meanwhile, the mulliken charge transfer values of C15, C23, O24 and O25 in PPD2CBA, C15, C23, O24 and O25 in PPD3CBA and C10, C23, O24 and O25 in PPD4CBA are pretty obvious (more positive) after adsorption (Table S7-S9), which indicates that electrons near the active adsorption site ($-COO^-$) are transferred and rearranged obviously during the adsorption process, and further verifies the complexation between carboxyl group and Hg(II).

Furthermore, Fig. S11 demonstrates the optimized structure of HgClOH complexed with the active site in solution in the presence of Cl^- and binding energy and Hg-O bond length in Table S10. The results show that the binding energy of the carboxyl group and HgClOH in PPD2CBA, PPD3CBA and PPD4CBA are -77.47, -81.98 and -83.25 $kJ \cdot mol^{-1}$, which also conforms to the following order: PPD4CBA > PPD3CBA > PPD2CBA, and is consistent with the experimental results of the adsorption capacity above.

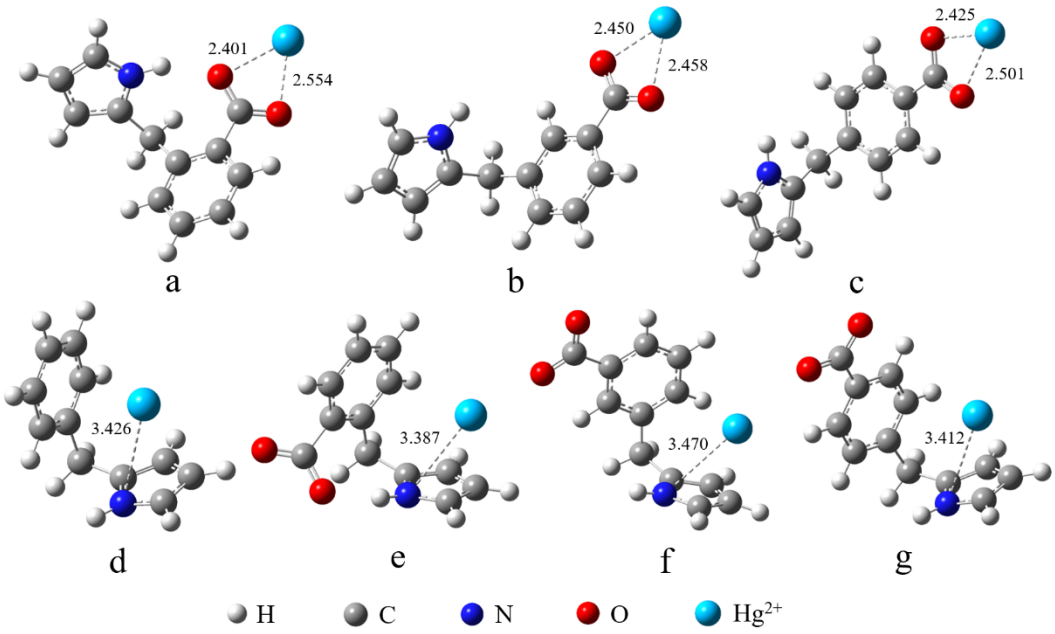

552

553 **Fig. 8.** Optimized geometries for the complexes of Hg(II) with carboxyl in PPD2CBA (a),

554 PPD3CBA (b) and PPD4CBA (c), and the complexes of Hg(II) with imino in PPDBA (d),

555 PPD2CBA (e) PPD3CBA (f) and PPD4CBA (g).

556 **Table 5.** Binding energy and bond length between mercury and adsorption active sites

Adsorbents	COO-Hg			NH-Hg	
	ΔE_{ad} (kJ·mol^{-1})	Bond length (Å)		ΔE_{ad} (kJ·mol^{-1})	Bond length (Å)
PPDBA	---	---	---	-57.29	3.426
PPD2CBA	-79.66	2.401	2.554	-67.96	3.387
PPD3CBA	-82.67	2.450	2.458	-66.18	3.470
PPD4CBA	-83.83	2.425	2.501	-68.54	3.412

557 **4. Conclusions**

558 In this work, we have demonstrated a strategy to design and tune the highly efficient and

559 selective removal of Hg(II) from aqueous solution by the poly(pyrrole methane)s with phenolic

carboxyl groups in the molecular skeleton (PPDCBAs). The saturation adsorption capacity of PPDCBAs with phenolic carboxyl groups for Hg(II) is much greater than that of PPDBA without carboxyl groups, indicating that carboxyl groups are the key to improving the adsorption capacity. Furthermore, the order of adsorption capacity of PPDCBAs was found to be: PPD4CBA > PPD3CBA > PPD2CBA. PPD4CBA has the maximum adsorption capacity for mercury of 1427 $mg \cdot g^{-1}$, and the fast kinetics for Hg(II) adsorption equilibrium within 100 min. Meanwhile, PPDCBAs have good adsorption selectivity for Hg(II) due to introducing a carboxyl group and steric hindrance. Moreover, the stronger affinity of PPDCBAs is ascribed to the complex of heavy metals and the carboxyl groups in the molecular skeleton. DFT calculation further proves that carboxyl and mercury have more negative adsorption energy, suggesting that carboxyl played a key role in mercury capture. It is also shown that PPDCBAs can maintain about 85% of the original adsorption capacity after ten adsorption-desorption cycles, which indicates the recyclability and stability of PPDCBAs for Hg(II) removal. In addition, PPDCBAs could adsorb and remove trace amounts of Hg(II) (10.8 $\mu g \cdot L^{-1}$) to meet the drinking water requirement specified by WTO (1 $\mu g \cdot L^{-1}$). Our results indicate that PPDCBAs have a strong potential for removing heavy metal ions from aqueous solutions.

CRediT authorship contribution statement

Zhenyu Wang: Conceptualization, Investigation, data curation, Writing-original draft preparation.

Yunpeng Liu: Data curation, Writing - review & editing.

Wenlong Zhang: Data curation, Writing - review & editing.

Yubing Wang: Data curation, Writing - review & editing.

Hao Xu: Writing - review & editing.

Liu Yang: Writing - review & editing.

Jiangtao Feng: Supervision, Writing - review & editing, Funding acquisition.

Bo Hou: Supervision, Writing - review & editing, Funding acquisition.

Mingtao Li: Software.

Wei Yan: Writing - review & editing.

Declaration of Competing Interest

The authors declare that they have no known competing financial interests or personal relationships that could have appeared to influence the work reported in this paper.

Acknowledgement

Jiangtao Feng acknowledges the National Natural Science Foundation of China (No. 52070155 and No. 51978569) and the Open Project of Jiangsu Engineering Laboratory of New Materials for Sewage Treatment and Recycling (No. SDGC2127). Bo Hou acknowledges the support from the Cardiff University, and Royal Society of Chemistry (No. E21-9668828170). The authors also acknowledge the financial support from the IEC\NSFC\211201-International

597 Exchanges 2021 Cost Share (NSFC) and the Instrumental Analysis Center of Xi'an Jiaotong
598 University for the help in SEM, XPS test and analysis.

599 **Appendix A. Supporting information**

600 Supplementary data associated with this article can be found in Supporting Information
601
602

603 **References**

604 Afaneh, A.T., Schreckenbach, G., Wang, F., 2012. Density functional study of substituted (-
605 SH, -S, -OH, -Cl) hydrated ions of Hg^{2+}. Theor. Chem. Acc. 131(4).

606 Aguila, B., Sun, Q., Perman, J.A., Earl, L.D., Abney, C.W., Elzein, R., Schlaf, R., Ma, S., 2017.
607 Efficient mercury capture using functionalized porous organic polymer. Adv. Mater.
608 29(31), 1700665.

609 Ahmad, H., BinSharfan, I., Khan, R.A., Alsalme, A., 2020. 3D Nanoarchitecture of
610 Polyaniline-MoS_2 Hybrid Material for Hg(II) Adsorption Properties. Polym. 12(11),
611 2731.

612 Al-Ghouti, M.A., Da'ana, D.A., 2020. Guidelines for the use and interpretation of adsorption
613 isotherm models: A review. J. Hazard. Mater. 393, 122383.

614 Alguacil, F.J., Escudero, E., 2020. La eliminación de metales tóxicos presentes en efluentes
615 líquidos mediante resinas de cambio iónico. Parte XII: Mercurio(II)/H^+/Lewatit SP112.
616 Rev. Metal. 56(1), 160.

617 Alguacil, F.J., López, F.A., 2020. Adsorption processing for the removal of toxic Hg(II) from
618 liquid effluents: advances in the 2019 year. Metals 10(3), 412.

619 Anirudhan, T.S., Divya, L., Ramachandran, M., 2008. Mercury(II) removal from aqueous
620 solutions and wastewaters using a novel cation exchanger derived from coconut coir pith
621 and its recovery. J. Hazard. Mater. 157(2-3), 620-627.

622 Bachand, S.M., Kraus, T.E.C., Stern, D., Liang, Y.L., Horwath, W.R., Bachand, P.A.M., 2019.
623 Aluminum- and iron-based coagulation for in-situ removal of dissolved organic carbon,

disinfection byproducts, mercury and other constituents from agricultural drain water. Ecol. Eng. 134, 26-38.

Bakker, J.M., Mac Aleese, L., Von Helden, G., Meijer, G., 2003. The infrared absorption spectrum of the gas phase neutral benzoic acid monomer and dimer. J. Chem. Phys. 119(21), 11180-11185.

Ballav, N., Das, R., Giri, S., Muliwa, A.M., Pillay, K., Maity, A., 2018. l-cysteine doped polypyrrole (PPy@L-Cyst): A super adsorbent for the rapid removal of Hg^{+2} and efficient catalytic activity of the spent adsorbent for reuse. Chem. Eng. J. 345, 621-630.

Bisla, V., Rattan, G., Singhal, S., Kaushik, A., 2020. Green and novel adsorbent from rice straw extracted cellulose for efficient adsorption of Hg (II) ions in an aqueous medium. Int. J. Bio.l Macromol. 161, 194-203.

Brown;, J.R., Bancroft;, G.M., Fyfe, W.S., 1979. Mercury removal from water by iron sulfide minerals. An Electron spectroscopy for chemical analysis (ESCA) study. Environ. Sci. Technol. 13, 1142-1144.

Caicedo Salcedo, O.D., Vargas, D.P., Giraldo, L., Moreno-Pirajan, J.C., 2021. Study of mercury [Hg(II)] adsorption from aqueous solution on functionalized activated carbon. ACS Omega 6(18), 11849-11856.

Chakrabarty, K., Saha, P., Ghoshal, A.K., 2010. Separation of mercury from its aqueous solution through supported liquid membrane using environmentally benign diluent. J. Membr. Sci. 350(1-2), 395-401.

644 Chen, J., Zhu, J., Wang, N., Feng, J., Yan, W., 2019. Hydrophilic polythiophene/SiO_2
645 composite for adsorption engineering: Green synthesis in aqueous medium and its
646 synergistic and specific adsorption for heavy metals from wastewater. Chem. Eng. J. 360,
647 1486-1497.
648 Chen, S.Y., Li, Z., Li, K., Yu, X.Q., 2021. Small molecular fluorescent probes for the detection
649 of lead, cadmium and mercury ions. Coord. Chem. Rev. 429, 213691.
650 Choi, H.Y., Bae, J.H., Hasegawa, Y., An, S., Kim, I.S., Lee, H., Kim, M., 2020. Thiol-
651 functionalized cellulose nanofiber membranes for the effective adsorption of heavy metal
652 ions in water. Carbohydr. Polym. 234, 115881.
653 Dai, D., Li, Z., Yang, J., Wang, C., Wu, J., Wang, Y., Zhang, D., Yang, Y., 2019.
654 Supramolecular assembly-induced emission enhancement for efficient mercury(II)
655 detection and removal. J. Am. Chem. Soc. 141(11), 4756-4763.
656 Dong, X., Ma, L.Q., Zhu, Y., Li, Y., Gu, B., 2013. Mechanistic investigation of mercury
657 sorption by Brazilian pepper biochars of different pyrolytic temperatures based on X-ray
658 photoelectron spectroscopy and flow calorimetry. Environ. Sci. Technol. 47(21), 12156-
659 12164.
660 Duan, W., Wang, J., Chang, L., Zhao, L., Tian, Z., Huang, Z., Huang, W., 2018. Adsorption of
661 mercury(II) from water by a novel sPAN fiber containing sulfhydryl, carboxyl and amino
662 groups. RSC Adv. 8(67), 38259-38269.
663 Elovich, S.Y., Larinov, O.G., 1962. Theory of adsorption from solutions of non electrolytes on
664 solid (I) equation adsorption from solutions and the analysis of its simplest form,(II)

verification of the equation of adsorption isotherm from solutions. Izv. Akad. Nauk. SSSR, Otd. Khim. Nauk 2(2), 209-216.

Freundlich, H., 1907. Über die Adsorption in Lösungen. 57U(1), 385-470.

Fu, K., Liu, X., Lv, C., Luo, J., Sun, M., Luo, S., Crittenden, J.C., 2022. Superselective Hg(II) Removal from Water Using a Thiol-Laced MOF-Based Sponge Monolith: Performance and Mechanism. Environ. Sci. Technol. 56(4), 2677-2688.

Fu, L., Wang, S., Lin, G., Zhang, L., Liu, Q., Fang, J., Wei, C., Liu, G., 2019. Post-functionalization of UiO-66-NH_2 by 2,5-Dimercapto-1,3,4-thiadiazole for the high efficient removal of Hg(II) in water. J. Hazard. Mater. 368, 42-51.

Fu, T., Niu, Y., Zhou, Y., Wang, K., Mu, Q., Qu, R., Chen, H., Yuan, B., Yang, H., 2019. Adsorption of Mn(II) from aqueous solution by silica-gel supported polyamidoamine dendrimers: Experimental and DFT study. J. Taiwan Inst. Chem. Eng. 97, 189-199.

Fu, Y., Sun, Y., Chen, Z., Ying, S., Wang, J., Hu, J., 2019. Functionalized magnetic mesoporous silica/poly(m-aminothiophenol) nanocomposite for Hg(II) rapid uptake and high catalytic activity of spent Hg(II) adsorbent. Sci. Total Environ. 691, 664-674.

Gao, X., Li, M., Zhao, Y., Zhang, Y., 2019. Mechanistic study of selective adsorption of Hg^{2+} ion by porous alginate beads. Chem. Eng. J. 378, 122096.

Ge, H., Du, J., 2020. Selective adsorption of Pb(II) and Hg(II) on melamine-grafted chitosan. Int. J. Bio.l Macromol. 162, 1880-1887.

Gupta, R., Gupta, S.K., Pathak, D.D., 2019. Selective adsorption of toxic heavy metal ions using guanine-functionalized mesoporous silica [SBA-16-g] from aqueous solution. Microporous Mesoporous Mater. 288, 109577.

Hall, K.R., L.C. Eagleton, A. Acrivos, Vermeulen, T., A. Acrivos, Vermeulen, T., 1966. Pore- and solid-diffusion kinetics in fixed-bed adsorption under constant-pattern conditions. Ind. Eng. Chem. Fundam. 5(2), 212-223.

Henneberry, Y.K., Kraus, T.E., Fleck, J.A., Krabbenhoft, D.P., Bachand, P.M., Horwath, W.R., 2011. Removal of inorganic mercury and methylmercury from surface waters following coagulation of dissolved organic matter with metal-based salts. Sci. Total Environ. 409(3), 631-637.

Holmes, P., James, K.A., Levy, L.S., 2009. Is low-level environmental mercury exposure of concern to human health? Sci. Total Environ. 408(2), 171-182.

I.D.Reva, S.G.Stepanian, 1995. An infrared study on matrix-isolated benzoic acid. J. Mol. Struct. 349, 337-340.

Jainae, K., Sukpirom, N., Fuangswasdi, S., Unob, F., 2015. Adsorption of Hg(II) from aqueous solutions by thiol-functionalized polymer-coated magnetic particles. J. Ind. Eng. Chem. 23, 273-278.

Ji, Y., Zhang, W., Yang, H., Ma, F., Xu, F., 2021. Green synthesis of poly(pyrrole methane) for enhanced adsorption of anionic and cationic dyes from aqueous solution. J. Colloid Interface Sci. 590, 396-406.

Kenawy, I.M., Hafez, M.A.H., Ismail, M.A., Hashem, M.A., 2018. Adsorption of Cu(II), Cd(II), Hg(II), Pb(II) and Zn(II) from aqueous single metal solutions by guanyl-modified cellulose. Int. J. Bio.l Macromol. 107, 1538-1549.

Lawrance, G.A., 2013. Introduction to coordination chemistry. John Wiley & Sons.

Leus, K., Perez, J.P.H., Folens, K., Meledina, M., Van Tendeloo, G., Du Laing, G., Van Der Voort, P., 2017. UiO-66-$(SH)_2$ as stable, selective and regenerable adsorbent for the removal of mercury from water under environmentally-relevant conditions. Faraday Discuss. 201, 145-161.

Li, B., Li, M., Zhang, J., Pan, Y., Huang, Z., Xiao, H., 2019. Adsorption of Hg (II) ions from aqueous solution by diethylenetriaminepentaacetic acid-modified cellulose. Int. J. Bio.l Macromol. 122, 149-156.

Li, B., Ye, L., Peng, E., Tan, Z., 2015. Synthesis, conductivity and photophysical properties of soluble low bandgap poly{(3-butyryl)pyrrole-[2,5-diyl(p-hydroxybenzylidene)]}. Synth. Met. 202, 33-38.

Li, B., Zhang, Y., Ma, D., Shi, Z., Ma, S., 2014. Mercury nano-trap for effective and efficient removal of mercury(II) from aqueous solution. Nat. Commun. 5, 5537.

Lin, C., Luo, W., Luo, T., Zhou, Q., Li, H., Jing, L., 2018. A study on adsorption of Cr (VI) by modified rice straw: Characteristics, performances and mechanism. J. Cleaner Prod. 196, 626-634.

723 Lin, G., Hu, T., Wang, S., Xie, T., Zhang, L., Cheng, S., Fu, L., Xiong, C., 2019. Selective
724 removal behavior and mechanism of trace Hg(II) using modified corn husk leaves.
725 Chemosphere 225, 65-72.
726 Liu, Y., Zhang, W., Zhao, C., Wang, H., Chen, J., Yang, L., Feng, J., Yan, W., 2019. Study on
727 the synthesis of poly(pyrrole methane)s with the hydroxyl in different substituent position
728 and their selective adsorption for Pb^{2+}. Chem. Eng. J. 361, 528-537.
729 Lu, X., Huangfu, X., Ma, J., 2014. Removal of trace mercury(II) from aqueous solution by in
730 situ formed Mn-Fe (hydr)oxides. J. Hazard. Mater. 280, 71-78.
731 Luo, F., Chen, J.L., Dang, L.L., Zhou, W.N., Lin, H.L., Li, J.Q., Liu, S.J., Luo, M.B., 2015.
732 High-performance Hg^{2+} removal from ultra-low-concentration aqueous solution using
733 both acylamide-and hydroxyl-functionalized metal-organic framework. J. Mater. Chem.
734 A 3(18), 9616-9620.
735 Lyu, W., Yu, M., Feng, J., Yan, W., 2019. Facile synthesis of coral-like hierarchical polyaniline
736 micro/nanostructures with enhanced supercapacitance and adsorption performance.
737 Polym. 162, 130-138.
738 Marenich, A.V., Cramer, C.J., Truhlar, D.G., 2009. Universal Solvation Model Based on Solute
739 Electron Density and on a Continuum Model of the Solvent Defined by the Bulk Dielectric
740 Constant and Atomic Surface Tensions. The Journal of Physical Chemistry B 113(18),
741 6378–6396.

742 Monahan, F.J., German, J.B., Kinsella, J.E., 1995. Effect of pH and Temperature on Protein
743 Unfolding and Thiol/Disulfide Interchange Reactions during Heat-Induced Gelation of
744 Whey Proteins. J. Agric. Food Chem. 43, 46-52.
745 Mungray, A.A., Murthy, Z.V.P., 2012. Comparative performance study of four nanofiltration
746 membranes in the separation of mercury and chromium. Ionics 18(8), 811-816.
747 Nasimi, S., Baghdadi, M., Dorosti, M., 2020. Surface functionalization of recycled
748 polyacrylonitrile fibers with ethylenediamine for highly effective adsorption of Hg(II)
749 from contaminated waters. J. Environ. Manage. 270, 110883.
750 Nightingale, E.R., 1959. Phenomenological theory of ion solvation. Effective radii of hydrated
751 ions. J. Phys. Chem. 63(9), 1381-1387.
752 Oyetade, O.A., Skelton, A.A., Nyamori, V.O., Jonnalagadda, S.B., Martincigh, B.S., 2017.
753 Experimental and DFT studies on the selective adsorption of Pb^{2+} and Zn^{2+} from aqueous
754 solution by nitrogen-functionalized multiwalled carbon nanotubes. Sep. Purif. Technol.
755 188, 174-187.
756 Peng, Y., Liu, X., Gong, X., Li, X., Liu, Y., Leng, E., Zhang, Y., 2018. Enhanced Hg(II)
757 adsorption by monocarboxylic-acid-modified microalgae residuals in simulated and
758 practical industrial wastewater. Energy Fuels 32(4), 4461-4468.
759 Richard, J.H., Biester, H., 2016. Mercury removal from contaminated groundwater:
760 Performance and limitations of amalgamation through brass shavings. Water Res. 99, 272-
761 280.

762 Saleh, T.A., 2015. Isotherm, kinetic, and thermodynamic studies on Hg(II) adsorption from
763 aqueous solution by silica- multiwall carbon nanotubes. Environ. Sci. Pollut. Res. Int.
764 22(21), 16721-16731.
765 Skyllberg, U., Drott, A., 2010. Competition between disordered iron sulfide and natural organic
766 matter associated thiols for mercury(II)s-an EXAFS study. Environ. Sci. Technol. 44(4),
767 1254-1259.
768 Takjoo, R., Hayatolgheibi, S.S., Amiri Rudbari, H., 2016. Preparation, X-ray structure, spectral
769 analysis, DFT calculation and thermal study on palladium(II) coordination compound
770 with Schiff base derived from S-allyldithiocarbazate. Inorganica Chimica Acta 447, 52-
771 58.
772 Tellez, S.C., Costa, A.C., Jr., Mondragon, M.A., Ferreira, G.B., Versiane, O., Rangel, J.L.,
773 Lima, G.M., Martin, A.A., 2016. Molecular structure, natural bond analysis, vibrational
774 and electronic spectra, surface enhanced Raman scattering and Mulliken atomic charges
775 of the normal modes of [Mn(DDTC)2] complex. Spectrochim Acta A Mol Biomol
776 Spectrosc 169, 95-107.
777 Toru Yahagi, Fujii, A., Ebata, T., Mikami, N., 2001. Infrared spectroscopy of the OH stretching
778 vibrations of jet-cooled salicylic acid and its dimer in S_0 and S_1. J. Phys. Chem. A 105(47),
779 10673-10680.
780 Tran, H.N., You, S.J., Hosseini-Bandegharaei, A., Chao, H.P., 2017. Mistakes and
781 inconsistencies regarding adsorption of contaminants from aqueous solutions: A critical
782 review. Water Resrarch 120, 88-116.

783 Velempini, T., Pillay, K., 2019. Sulphur functionalized materials for Hg(II) adsorption: A
784 review. J. Environ. Chem. Eng. 7(5), 103350.
785 Wang, F., Lu, X., Li, X.Y., 2016. Selective removals of heavy metals (Pb^{2+}, Cu^{2+}, and Cd^{2+})
786 from wastewater by gelation with alginate for effective metal recovery. J. Hazard. Mater.
787 308, 75-83.
788 Wang, J., Guo, X., 2020. Adsorption kinetic models: Physical meanings, applications, and
789 solving methods. J. Hazard. Mater. 390, 122156.
790 Wang, X., Yang, L., Zhang, J., Wang, C., Li, Q., 2014. Preparation and characterization of
791 chitosan-poly(vinylalcohol)/bentonite nanocomposites for adsorption of Hg(II) ions.
792 Chem. Eng. J. 251, 404-412.
793 Worthington, M.J.H., Kucera, R.L., Albuquerque, I.S., Gibson, C.T., Sibley, A., Slattery, A.D.,
794 Campbell, J.A., Alboaiji, S.F.K., Muller, K.A., Young, J., Adamson, N., Gascooke, J.R.,
795 Jampaiah, D., Sabri, Y.M., Bhargava, S.K., Ippolito, S.J., Lewis, D.A., Quinton, J.S.,
796 Ellis, A.V., Johs, A., Bernardes, G.J.L., Chalker, J.M., 2017. Laying waste to mercury:
797 inexpensive sorbents made from sulfur and recycled cooking oils. Chemistry 23(64),
798 16219-16230.
799 Xu, Y., Chen, J., Chen, R., Yu, P., Guo, S., Wang, X., 2019. Adsorption and reduction of
800 chromium(VI) from aqueous solution using polypyrrole/calcium rectorite composite
801 adsorbent. Water Res. 160, 148-157.
802 Yan, X., Li, P., Song, X., Li, J., Ren, B., Gao, S., Cao, R., 2021. Recent progress in the removal
803 of mercury ions from water based MOFs materials. Coord. Chem. Rev. 443, 214034.

804 Zhang, C., Sui, J., Li, J., Tang, Y., Cai, W., 2012. Efficient removal of heavy metal ions by
805 thiol-functionalized superparamagnetic carbon nanotubes. Chem. Eng. J. 210, 45-52.
806 Zhang, J., Zhai, J., Zheng, H., Li, X., Wang, Y., Li, X., Xing, B., 2020. Adsorption, desorption
807 and coadsorption behaviors of sulfamerazine, Pb(II) and benzoic acid on carbon
808 nanotubes and nano-silica. Sci. Total Environ. 738, 139685.
809 Zhang, Y., Bland, G.D., Yan, J., Avellan, A., Xu, J., Wang, Z., Hoelen, T.P., Lopez-Linares,
810 F., Hatakeyama, E.S., Matyjaszewski, K., Tilton, R.D., Lowry, G.V., 2021. Amphiphilic
811 thiol polymer nanogel removes environmentally relevant mercury species from both
812 produced water and hydrocarbons. Environ. Sci. Technol. 55(2), 1231-1241.
813 Zhang, Z., Zhou, Q., Yuan, Z., Zhao, L., Dong, J., 2021. Adsorption of Mg^{2+} and K^{+} on the
814 kaolinite (0 0 1) surface in aqueous system: A combined DFT and AIMD study with an
815 experimental verification. Appl. Surf. Sci. 538.
816 Zhao, M., Huang, Z., Wang, S., Zhang, L., Zhou, Y., 2019. Design of l-Cysteine functionalized
817 UiO-66 MOFs for selective adsorption of Hg(II) in aqueous medium. ACS Appl. Mater.
818 Interfaces 11(50), 46973-46983.
819 Zhou, X., Zhou, X., 2014. The Unit Problem in the Thermodynamic Calculation of Adsorption
820 Using the Langmuir Equation. Chem. Eng. Commun. 201(11), 1459-1467.
821 Zhu, H., Shen, Y., Wang, Q., Chen, K., Wang, X., Zhang, G., Yang, J., Guo, Y., Bai, R., 2017.
822 Highly promoted removal of Hg(II) with magnetic $CoFe_2O_4@SiO_2$ core-shell
823 nanoparticles modified by thiol groups. RSC Adv. 7(62), 39204-39215.

824